Wide-Band Airborne Radar Operating Considerations for Low-Altitude Surveillance in the Presence of Specular Multipath

Joseph G. Teti, Jr., *Member, IEEE*

***Abstract*—Reliable detection of low-altitude platforms while simultaneously maintaining a desired search rate can be extremely difficult due to the presence of multipath. Wide-band operation in combination with frequency diversity is a sensible approach to not only mitigate, but in some cases exploit multipath channel characteristics. While a great deal of knowledge exists for characterizing the frequency dependencies of complicated multipath channels, relatively little attention has been given to examining how this knowledge could be exploited with wide-band radar sensors. The utilization of multipath channel characteristics is considered for the scenario of an airborne wide-band radar sensor performing low-altitude surveillance in a maritime environment. A brief overview of applicable multipath phenomenology is presented leading to a description of the propagation conditions selected for the construction of a representative channel. A generalized wide-band model of the sensor engagement applicable to the resolved and unresolved domains of the interference regime is utilized in combination with the simulated channel. Wide-band short pulse and linear frequency modulation waveforms are employed to consider waveform modulation characteristics in combination with desirable sensor bandwidth and frequency diversity for nominal operation at X-band. A brief discussion on implementation possibilities is also included.**

***Index Terms*—Multipath channels, wide-band radar.**

I. Introduction

Most surveillance radar applications typically desire 360° azimuth coverage. In some cases, a smaller azimuth angular sector may be acceptable for an individual sensor, with multiple sensors required to cover 360°. The usual figure of merit for a surveillance sensor is the search rate arising from the time resources necessary to yield the desired detection and angular resolution performance throughout the intended angular coverage sector. A number of practical considerations lead to a small number of apertures (often one) that cannot allow observing all angular directions at all times (e.g., a mechanically rotating or electronically scanning antenna). Consequently, the radar sensor's revisit rate must be carefully considered for the intended application with particular attention to detection and tracking of moving platforms. For the case of a single aperture airborne radar searching for low-altitude fast moving platforms, the sensor's revisit rate requirements must also consider the range dependent characteristics of multipath induced fading that is a function of operating frequency and illumination geometry. It is well known that when the multipath fading characteristics can be attributed to specular reflection (as is often the case in a maritime environment), the illumination of a low-altitude platform will result in situations of constructive and destructive interference at the sensor, where strong destructive interference can result in missed detection when revisit opportunities coincide with the deep fade conditions. Of course, constructive interference can enhance detection, but would not be sensibly relied on by a conservative assessment of system detection performance.

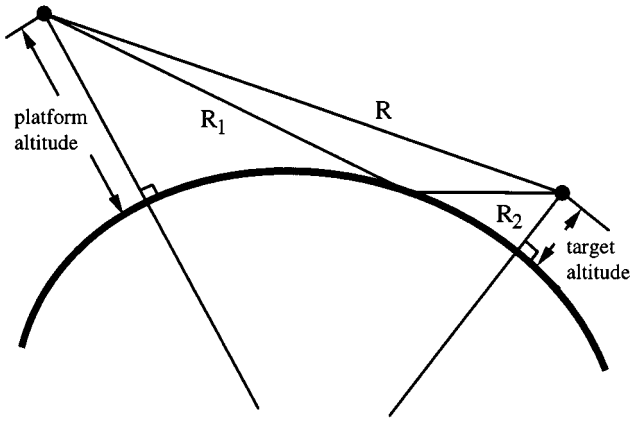

Fig. 1. Specular multipath illumination geometry.

For illustration, consider the illumination geometry shown in Fig. 1. The one-way direct path in combination with the two-way bounce path comprise four two-way propagation paths. The vector superposition of the four wavefronts arriving at the radar sensor can be expressed by the two-way voltage propagation factor

$$F^2 = |f(\varphi_d) + \rho f(\varphi_r) e^{-j\delta}|^2 \tag{1}$$

where $f(\varphi_d)$ and $f(\varphi_r)$ compensate for illumination angle offsets with respect to antenna main beam position with subscripts denoting the direct and reflected rays, ρ is the complex reflection coefficient, and δ is the relative phase between the direct and reflected propagation paths R and $R_1 + R_2$. A general discussion on the use of (1) can be found in many books on radar (e.g., [1]). The basic form of (1) accounts for the presence of constructive and destructive interference regions in accordance with the frequency-dependent relative phase. The frequency dependence of the multipath null positions can be appreciated by considering continuous-wave (CW) operation examining only

Manuscript received September 25, 1998; revised May 5, 1999. This work was supported in part by ONR under Contract N00014-96-C-0296.

The author is with the Lambda Science, Inc., Wayne, PA 19087-0238 USA.

Publisher Item Identifier S 0018-926X(00)01646-X.

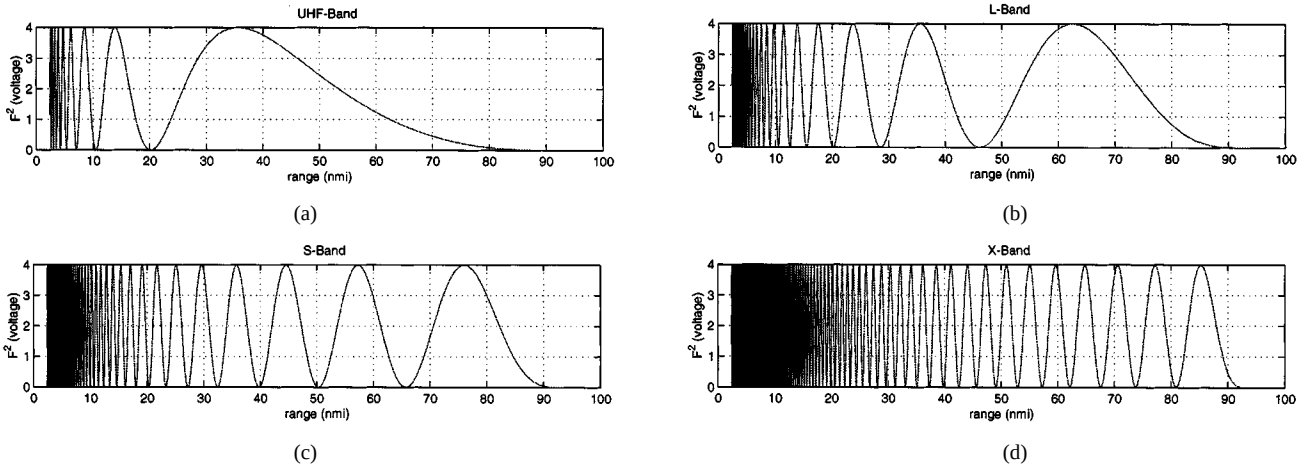

Fig. 2. Simplified multipath propagation factors for 5000 ft sensor altitude illuminating a platform at 30 ft altitude: (a) ultrahigh frequency (UHF)-band, (b) L-band, (c) S-band, and (d) X-band CW operation.

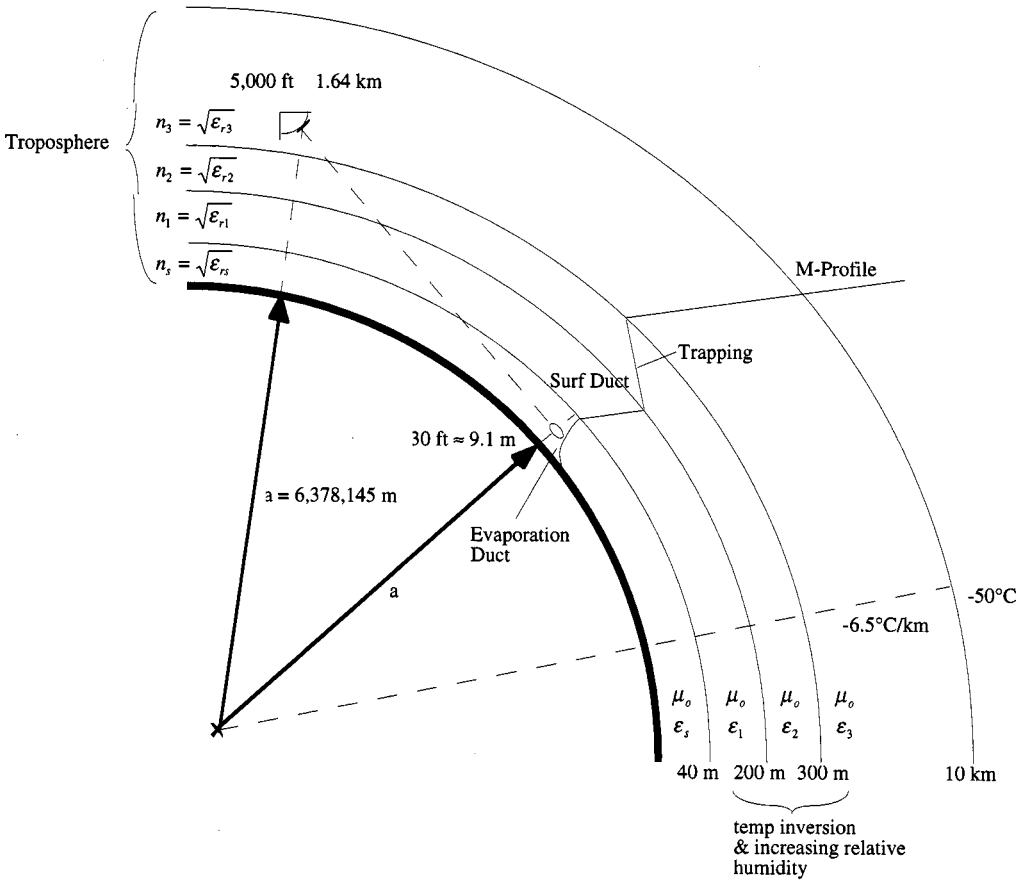

Fig. 3. Troposphere description and sensor illumination scenario in the presence of ducting.

the explicit phase factor in (1) (with all other quantities ≈ 1). For example, Fig. 2 illustrates multipath null position locations for UHF, L, S, and X-band operation. Interpreting range as time delay in Fig. 2, it is apparent how low-altitude detection and tracking in a multipath environment can pose a significant challenge to surveillance radar sensors. The operational evidence of frequently encountering coherent multipath in a maritime environment motivates an assessment of what can be done to mitigate or possibly exploit this type of channel. The frequency dependency of the multipath null positions suggests the consideration of using a wide-band radar capable of frequency diversity to mitigate and possibly exploit the multipath channel. From practical considerations, X-band operation is selected for the model radar sensor considered in this work. Upon examining Fig. 2, it is clear that the propagation factor interference pattern maxima and minima occur more frequently in range with increasing operating frequency. This observation indicates that the frequency diversity resources (percentage bandwidth) required to mitigate or exploit the coherent interference effects decrease with increasing operating frequency. In addition, operation at X-band

allows aperture sizes that are compatible with a large variation of airborne platforms, and the required wide-band hardware technologies are either already or becoming increasingly available.

This paper describes the utilization of wide-band frequency diversity to mitigate and exploit specular multipath channel characteristics encountered by an airborne sensor performing low-altitude surveillance in a maritime environment. The subsequent analysis considers a physically representative channel and realistic wide-band radar sensor operating characteristics. Section II provides a brief overview of propagation in the troposphere and ocean surface scattering leveraging the vast open literature information that is available. Section III details the subject model platform/sensor operating characteristics. Section IV describes transmit frequency diversity considerations and multipath channel mitigation and exploitation. Overall conclusions and a discussion on implementation possibilities are provided in Section V.

II. Tropospheric Propagation Channel Background

The troposphere is the region of the earth's atmosphere that extends from the surface to an altitude of about 10 km (∼33 000 ft) and the illumination scenarios for airborne surveillance are in most cases confined to tropospheric propagation effects. Propagation in the troposphere has been studied for about the last half century and continues to be an active area of research (e.g., [2]–[8]). Range dependent properties of tropospheric propagation are generally separated into three regions: 1) interference; 2) intermediate; and 3) diffraction [2]. Within the horizon, the propagation phenomena associated with the interference region are characterized by four refractive conditions; subrefraction, standard, superrefraction, and trapping (ducting). Each of these conditions can occur in combination and the presence of tropospheric scattering (troposcatter) effects that arise from regions that contain turbulent fluctuation in the index of refraction are also possible. This work explicitly considers the coherent interference regime.

The index of refraction (or relative dielectric) in the troposphere varies with altitude, range (i.e., position) and time. The relative dielectric of the troposphere is known to be a function of humidity, pressure and temperature. The temporal variations of the environmental conditions take place on relatively large time scales (hours, days, etc.) that support the existence of coherent propagation phenomena, and in many applications the observations generally take place on time scales that are small enough (minutes, seconds, etc.) for the conditions to be considered constant. For the propagation conditions considered here, the refractive index is assumed constant during a sensor's coherent processing interval (CPI). Note that if the temporal stability of the refractive index is not sufficient to support the existence of coherent interference, then methods to mitigate or exploit the effects are not applicable.

The spatial variation of the index of refraction is generally larger with altitude than range and, in many cases, the range variation can be sensibly neglected. Accordingly, the refractivity and the modified refractivity are given by $N(\mathbf{r},t) = (n(\mathbf{r},t) - 1)\times 10^6 \approx N(\mathbf{r})$ and $M(\mathbf{r},t) = N(\mathbf{r},t) + (h/a)\times 10^6 \approx M(\mathbf{r})$, respectively, where h is the altitude above the earth and a is the earth's radius described in an earth-centered spherical geometry. The ray curvature (bending) associated with propagation in the standard atmosphere is considered to be the result of a stable and well-mixed dielectric profile characterized by an index of

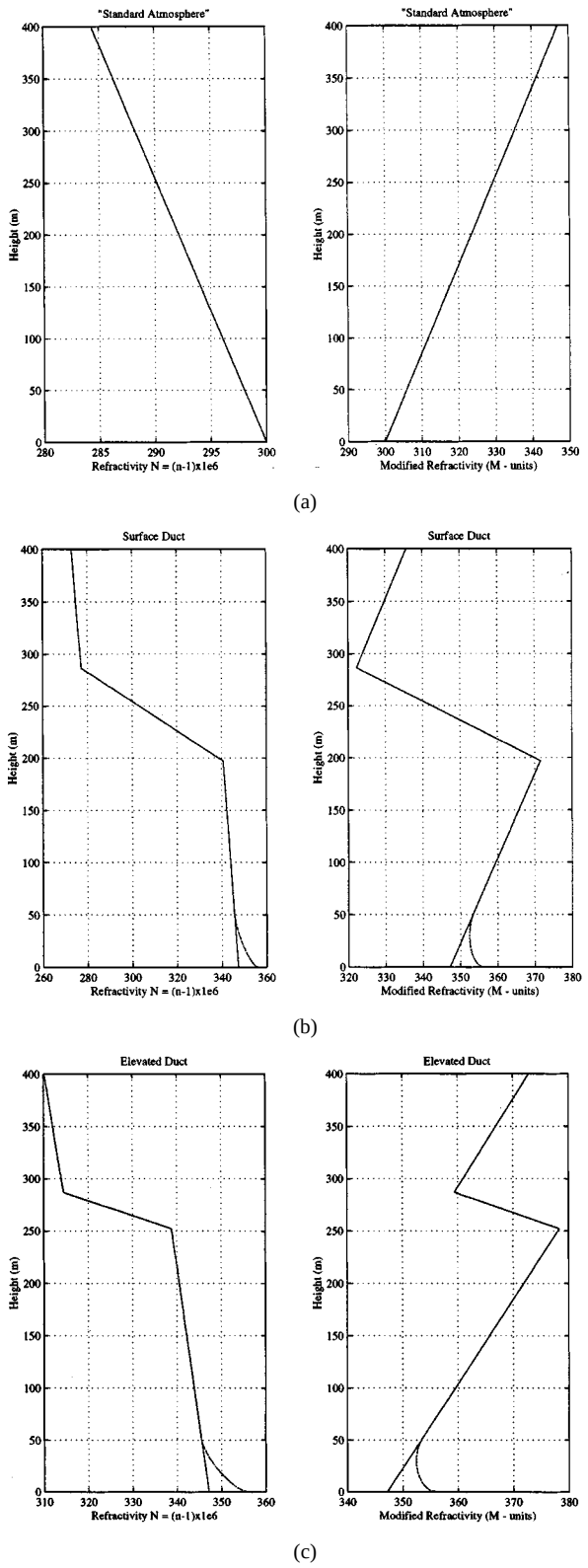

Fig. 4. Sample refractivity profiles. (a) Standard. (b) Surface duct. (c) Elevated duct.

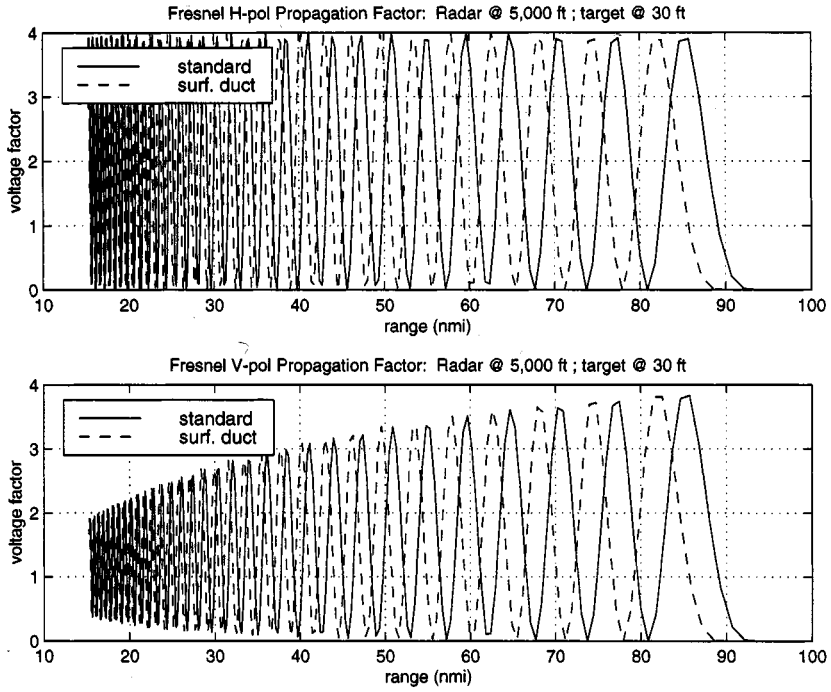

Fig. 5. Predominant ducting effects on coherent interference.

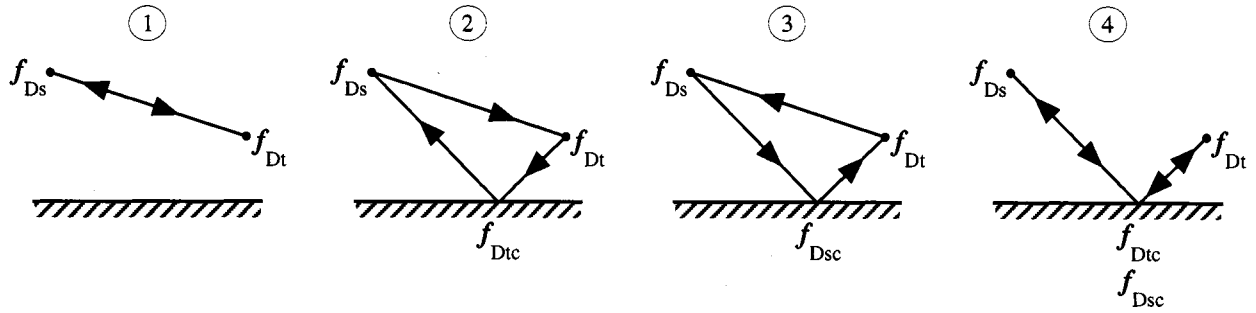

Fig. 6. Multipath components corresponding to (4).

refraction that varies exponentially with altitude. Nonstandard types of ray curvature are the result of anomalous propagation caused by index of refraction spatial distributions that deviate from the exponential model for the standard atmosphere. The low-altitude variation of the exponential model is essentially linear in the troposphere where ducting conditions are common in a maritime environment. When ducting conditions exist, they can often dominate the propagation conditions. Fig. 3 is a pictorial description of a representative troposphere that includes details on the radar sensor illumination geometry considered in this work (the altitude information is used throughout).

The relationship between the refractivity and modified refractivity are quantified by the examples shown in Fig. 4. Fig. 4(a) represents the standard atmosphere and Fig. 4(b) and (c) represent a surface duct and elevated duct, respectively. Figs. 3, 4(b) and (c) also illustrate the presence of the evaporation duct given by the nonlinear section visible at the base of the altitude profiles. The evaporation duct is almost always present in a maritime environment and is caused by the rapid decrease in mois-

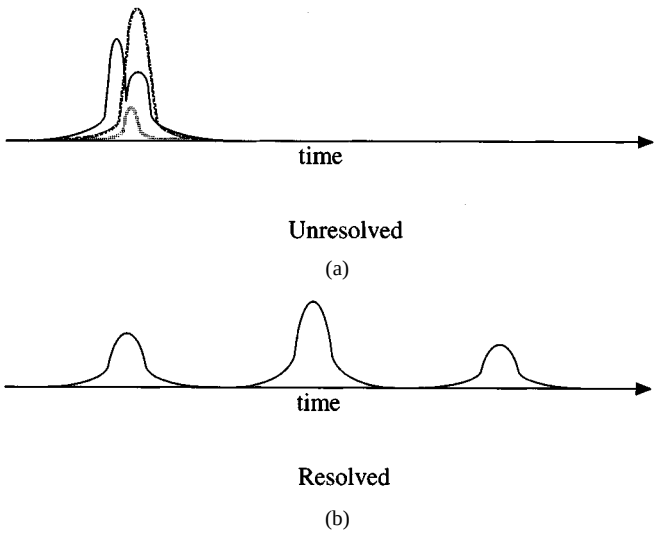

Fig. 7. Unresolved and resolved domains of the interference regime associated with (6).

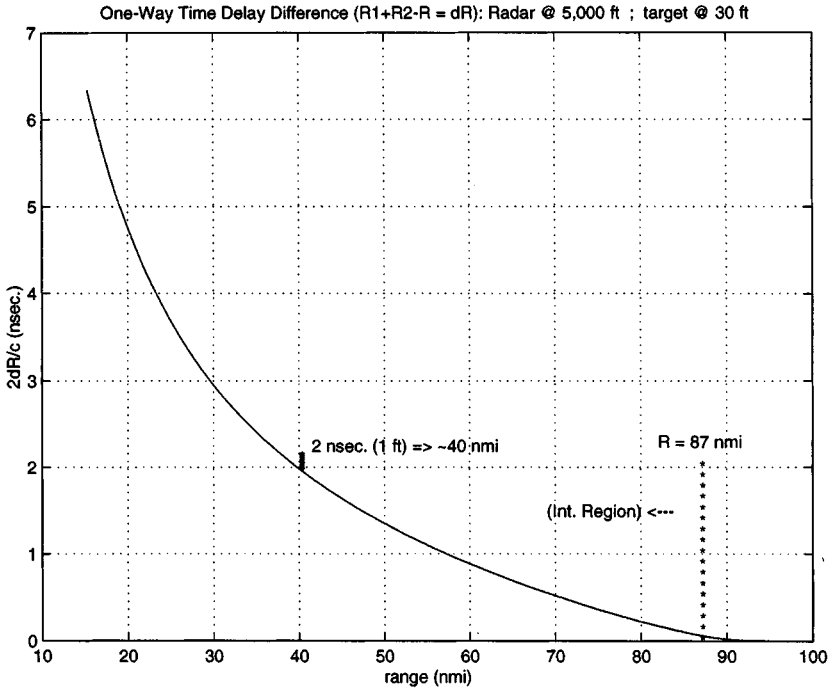

Fig. 8. Multipath range delay resolution for the interference regime.

ture content in the atmospheric layer just above the ocean's surface (see [4] for a further discussion).

For the conditions of anomalous propagation, solution to the Helmholtz wave equation can be formulated. For tropospheric propagation, solutions are commonly determined numerically under the parabolic approximation, readily retaining only the forward propagating component of the field (e.g., [6]). Full wave solutions without the parabolic approximation can also be implemented at the expense of increased computational complexity (e.g., [7]). The literature is rich with problem scenarios where numerically solving the wave equation is unavoidable [5]–[8]. However, under propagation conditions that can be described by constant geometrical wave fronts $\zeta(\mathbf{r})$, the Eikonal equation

$$|\nabla\zeta(\mathbf{r})|^2 = \left(\frac{\partial\zeta}{\partial x}\right)^2 + \left(\frac{\partial\zeta}{\partial y}\right)^2 + \left(\frac{\partial\zeta}{\partial z}\right)^2 = n^2(\mathbf{r}) \qquad (2)$$

is the sensible tool of choice and is very effective in capturing the propagation effects that must be considered in this work. With $n(\mathbf{r})\ d\mathbf{r}/ds = \nabla\zeta(\mathbf{r})$, (2) can be used to show $nr\ \cos(\varphi) =$ *constant* (Snell's Law). For the situation shown in Fig. 4(a) the desired form is given by $n_s a\ \cos(\varphi_o) = n(h)(a+h)\cos(\varphi)$. The index of refraction is taken to have an altitude dependency given by the linear form $n(h) = n_s + m_k h/a$, where n_s designates the index of refraction at the earth's surface and m_k is the slope factor of the index of refraction's altitude profile for the kth layer. The kth layer dependency readily allows the effects of ducting to be considered as a piecewise continuous trilinear altitude profile ignoring the evaporation duct. The implications of ignoring the evaporation duct will be addressed later. When considering $n(h)$, it is customary (unless known from measurement) to assume n_s is unity, resulting in the determination of an "effective" earth radius given by $a_{ek} = a/|1+m_k|$ for the kth layer. The use of an effective earth radius accounts for ray curvature as a modified line-of-site (LOS) distance determined for an effective spherical earth. Thus, the correct ray length (propagation distance) information can be determined from geometry using an effective earth radius. For the case of a single layer described by the standard atmosphere model, $m = -0.25$ corresponds to $a_e = (4/3)a$ (commonly referred to as the "four thirds earth" model).

The simple trilinear altitude profile of the index of refraction is substantiated by a considerable amount of experimental evidence [4], [5]. This work requires only a representative sample of ducting conditions to quantify the effects on the propagation characteristics of the interference regime. The surface duct characteristics shown in Fig. 4(b) are based on measurements reported in [5]. For the trilinear refractivity profile of Fig. 4(b) the slope factors for the individual altitude layers are $m_1 = -0.2118$, $m_2 = -4.5104$ and $m_3 = -0.2422$, where increasing subscripts correspond to increasing altitude. The effective earth radii that correspond to the altitude layers are used to determine the length of individual ray sections. The total ray lengths are computed as a superposition of the individual ray sections. The ray length calculations must be repeated as a function of range (or grazing angle) for the considered case of fixed altitude illumination. With ray length information that accounts for ducting conditions, the predominant effects on coherent interference that are of concern for frequency diversity considerations can be examined using the propagation factor given by (1). For example, Fig. 5 illustrates the coherent interference characteristics for horizontal and vertical polarization using the refractivity profiles of Fig. 4(a) and (b). The polarization dependency is the result of including the Fresnel reflection coefficient for sea water with (1), and has not been introduced by the ducting effect considerations. Fig. 5 clearly illustrates that ducting effects on

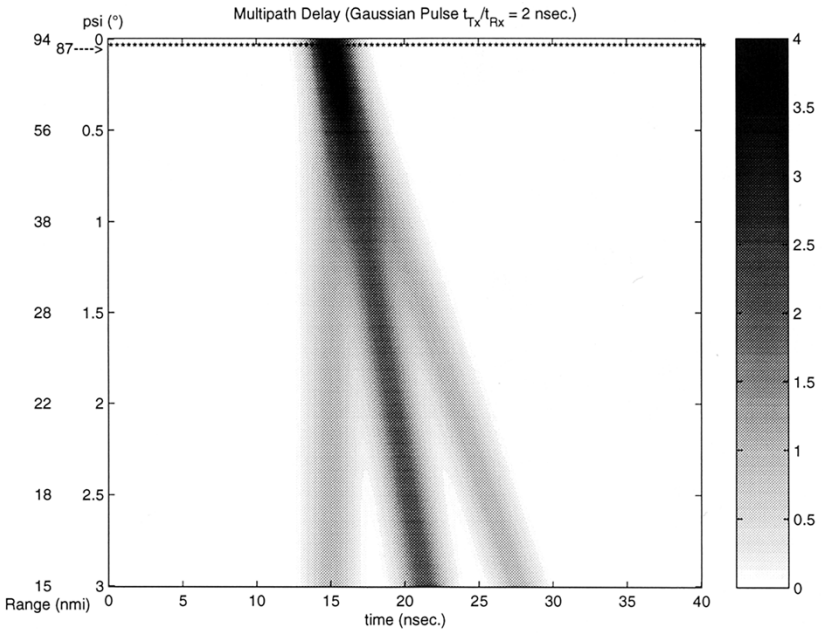

(a)

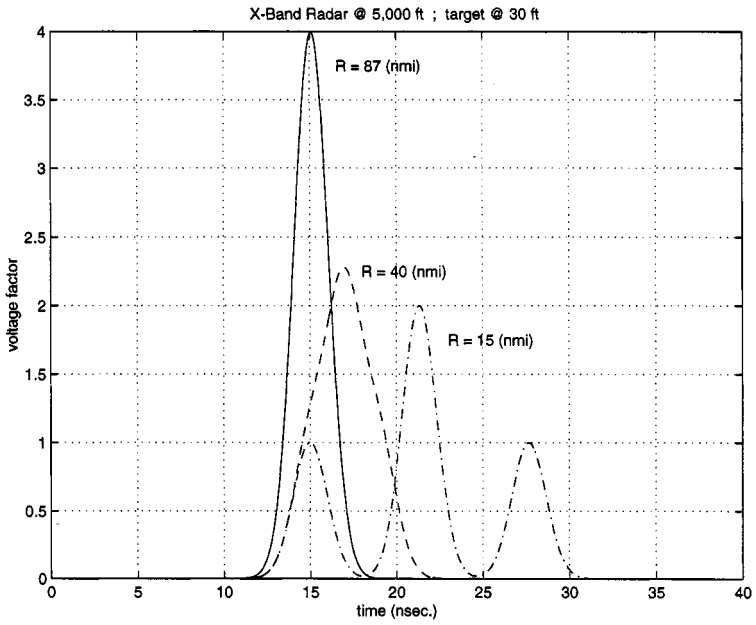

(b)

Fig. 9. Coherent interference reference description of the multipath channel test case illustrating the envelope of the propagation factor; (b) is comprised of range cuts from (a).

coherent interference result in a range shift in the locations of relative maxima and minima, which is consistent with measured observations [5]. Consequently, frequency diversity techniques will not find it any more difficult to deal with ducting conditions as they do with nonducting conditions, provided that the existence of coherent interference can also be supported in both cases. Furthermore, the effects of the evaporation duct can be considered in the same fashion.

Appendix A contains the ocean surface scattering characteristics for the bounce path needed to complete a sufficient physical representation of a maritime multipath channel.

III. Model Sensor Operation and Channel Characteristics

The illumination geometry for the model sensor is described in Fig. 3. The tunable band of the model sensor available for hosting frequency diversity is 8–14 GHz. The instantaneous bandwidth is 500 MHz. The analysis considers a 2 ns Gaussian pulse waveform on transmit and receive and a linear frequency modulation (FM) waveform with a 4-μs transmit duration compressed to 2 ns with receive matched filtering. In a general sense, for a wide-band transmit waveform described by

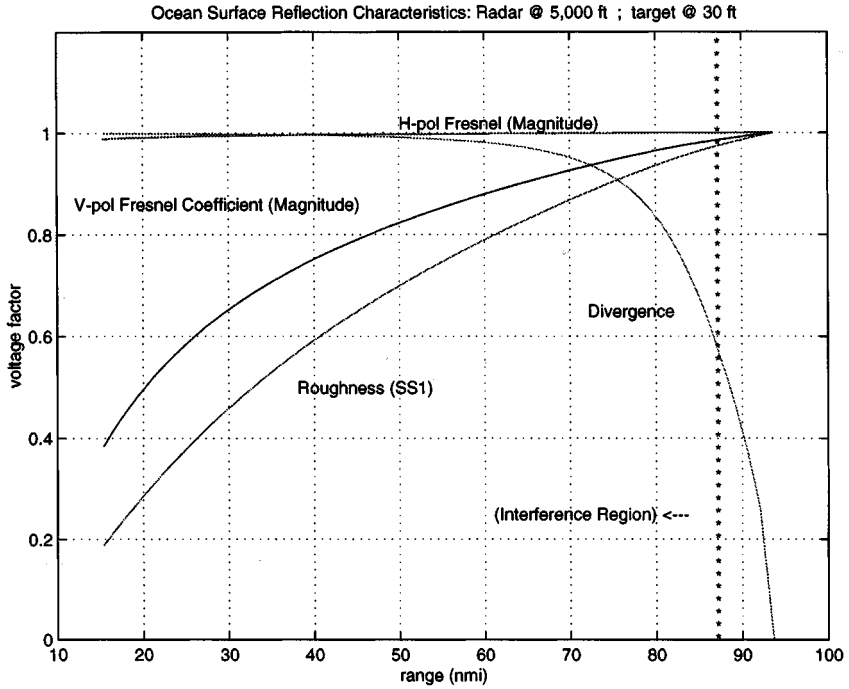

Fig. 10. The physical characteristics of the multipath channel test case.

$s(t)e^{-j2\pi f_c t}$ with carrier frequency f_c and pulse modulation $s(t)$, the received signal is given by

$$r(t) = \sum_{i=1}^{4} p_i(t - T_i) \tag{3}$$

where the path components are

$$p_1(t - T_1) = f(\varphi_d)[f(\varphi_d)s(t - T_1)e^{-j2\pi f_{D_s} t} * \xi_d(t)e^{-j2\pi f_{D_t} t}] \tag{4a}$$

$$p_2(t - T_2) = f(\varphi_b)[(f(\varphi_d)s(t - T_2)e^{-j2\pi f_{D_s} t} * \xi_b(t)e^{-j2\pi f_{D_s} t}) * \rho_{rms}(-t)e^{-j2\pi f_{D_{tc}} t}] \tag{4b}$$

$$p_3(t - T_3) = f(\varphi_d)[(f(\varphi_b)s(t - T_3)e^{-j2\pi f_{D_s} t} * \rho_{rms}(t)e^{-j2\pi f_{D_{sc}} t}) * \xi_b(t)e^{-j2\pi f_{D_t} t}] \tag{4c}$$

and (4d), shown at the bottom of the page, at baseband (after down conversion and before matched filtering). A pictorial description of (4) is provided in Fig. 6. The time dependence in (4) is associated with range where T_i denotes roundtrip time delay. Also included in (4) are Doppler offsets, complex antenna pattern weights, and an extended scatterer description with bistatic radar cross section proportional to $|\xi|^2$. Note that with the appropriate assumptions, (1) can be deduced from (3) with (4). In terms of radar system observables, the roundtrip time delays T_2 and T_3 are equal and the two single bounce paths (shown in Fig. 6) cannot be temporally resolved. Conventional matched filtering an observable version of (3) with $h(t)$ is given by

$$y(t) = \hat{r}(t) * h(t) = \left(\sum_{i=1}^{3} \hat{p}_i(t - T_i)\right) * h(t) = \sum_{i=1}^{3} (\hat{p}_i(t - T_i) * h(t)) \tag{5}$$

where $\hat{p}_1 = p_1$, $\hat{p}_2 = p_2 + p_3$, and $\hat{p}_3 = p_4$. Considering the pulse duration characteristics of the waveform with the equivalent linear forms on the right-hand side (RHS) of (5), it is clear that two multipath interference domains exist, could be excited and processed differently to mitigate or exploit the channel characteristics. The multipath model form of (5) is given by

$$y(t) = \left(\sum_{i=3}^{3} \hat{p}_i(t - T_i)\right) * h_u(t), \qquad unresolved\,domain \tag{6a}$$

for the temporally unresolved case where $h_u(t)$ need not be equivalent to $h(t)$ and

$$y(t) = \sum_{i=1}^{3} (\hat{p}_i(t - T_i) * h_i(t)), \qquad resolved\,domain \tag{6b}$$

for the temporally resolved case where none of the $h_i(t)$ need be equivalent to $h(t)$. The two domains described in (6) are illustrated in Fig. 7. The performance in the unresolved domain

$$p_4(t - T_4) = f(\varphi_b)[((f(\varphi_b)s(t - T_4)e^{-j2\pi f_{D_t} t} * \rho_{rms}(t)e^{-j2\pi f_{D_{sc}} t})\xi_{2b}(t)e^{-j2\pi f_{D_t} t} * \rho_{rms}(-t)e^{-j2\pi f_{D_{tc}} t}] \tag{4d}$$

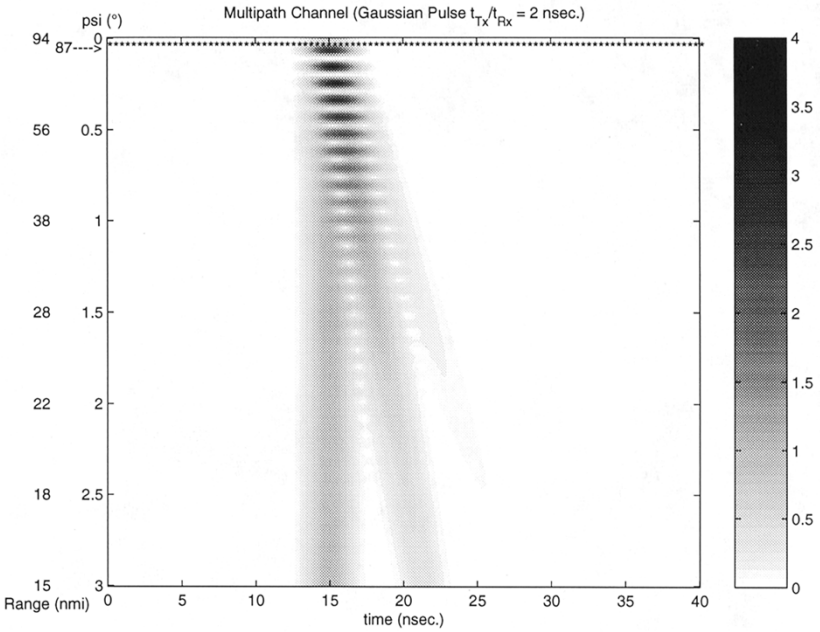

(a)

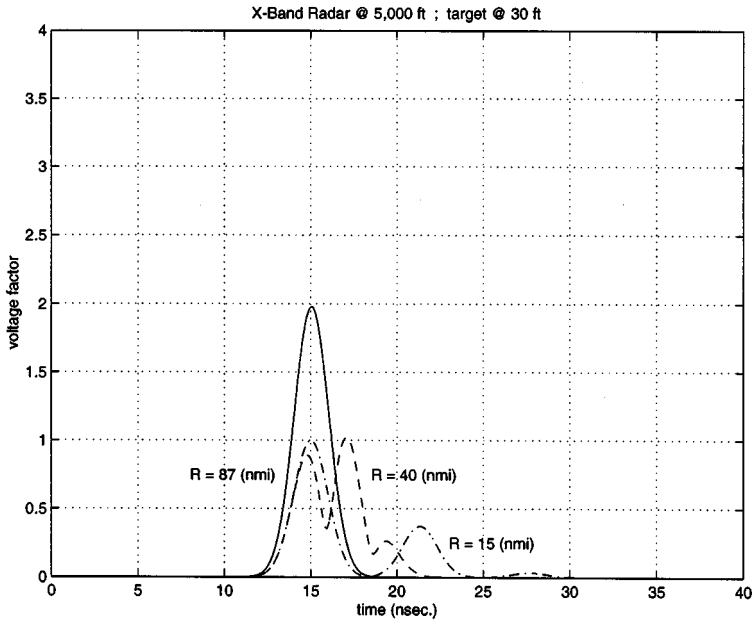

(b)

Fig. 11. Coherent interference reference description of the multipath channel test case for the short Gaussian pulse waveform; (b) is comprised of range cuts from (a).

shown in Fig. 7(a) is influenced through transmit frequency diversity.

The model sensor's range resolution establishes the transition boundary between the unresolved and resolved domains of the interference regime. A wide-band information bandwidth of 500 MHz is selected for the model sensor corresponding to ∼2 ns resolution (∼1-ft range resolution). Fig. 8 illustrates that the separate multipath returns should become discernible at ∼40 nmi for selected model sensor operating characteristics. Fig. 8 also indicates a range extent of ∼87 nmi corresponding to the grazing angle extent of the interference regime described by (A.5), and many of the subsequent graphical results retain the inclusion of this indicator.

An ideal yet unrealistic description of the specular multipath channel under consideration is shown in Fig. 9 for a 2 ns Gaussian pulse. Fig. 9 is unrealistic because it represents lossless reflection and constructive coherent interference throughout the range extent (i.e., the envelope of the propagation factor for perfect reflection). Fig. 9(a) illustrates a 40 ns window that is delay aligned to 15 ns over the range extent shown on the abscissa; the range position and corresponding grazing angle are shown on the ordinate. Also shown is

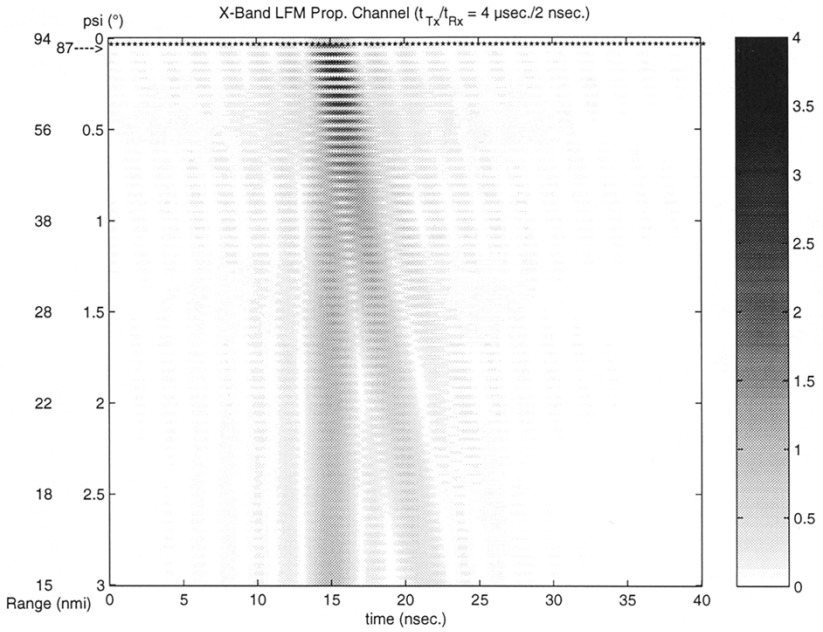

(a)

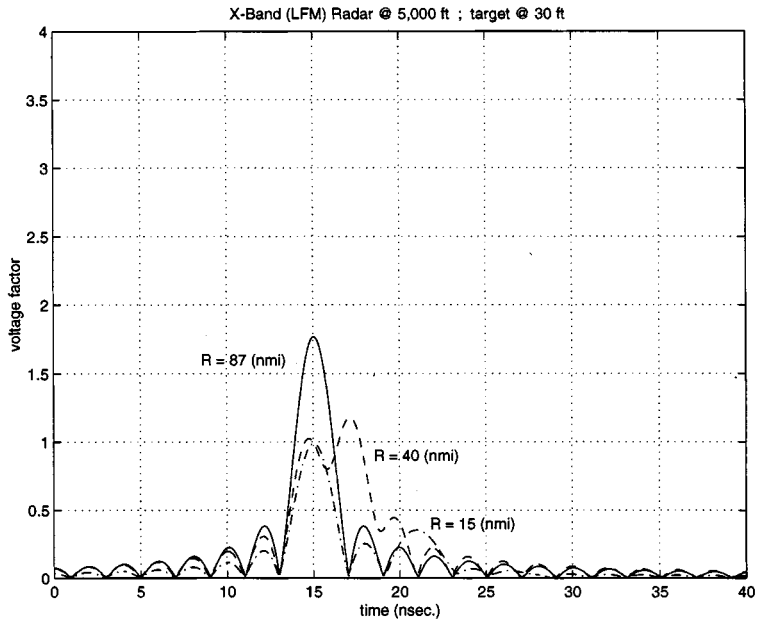

(b)

Fig. 12. Coherent interference reference description of the multipath channel test case for the linear FM pulse waveform after compression; (b) is comprised of range cuts from (a).

the geometrical optic limit of the interference regime at 87 nautical miles (from (A.5)). Fig. 9(b) illustrates range cuts through Fig. 9(a) at locations corresponding to the unresolved, transition, and resolved domains of the interference regime. The channel characterization provided by Fig. 9 serves as a reference to contrast more realistic characterizations of the multipath channel. The format of this figure is used in subsequent graphical results.

Fig. 10 summarizes the ingredients chosen to construct a physically representative channel for the low flyer illumination geometry described in Fig. 3. The test case multipath channel utilizes a composite complex reflection coefficient (A.1) computed for horizontal polarization and sea state one (SS1) with the factors illustrated in Fig. 10. Only SS1 is considered for illustration because it is consistent with the conditions necessary for a severe multipath channel to exist. As the ocean surface roughness increases, the strength and deleterious effects of the multipath diminish. Accordingly, the need to mitigate and the potential to benefit from exploiting multipath effects also diminishes. However, the ocean and atmospheric conditions necessary for the presence of deleterious multipath effects occur fairly often. All subsequent sensor operating considerations are quantified with respect to the test case multipath channel.

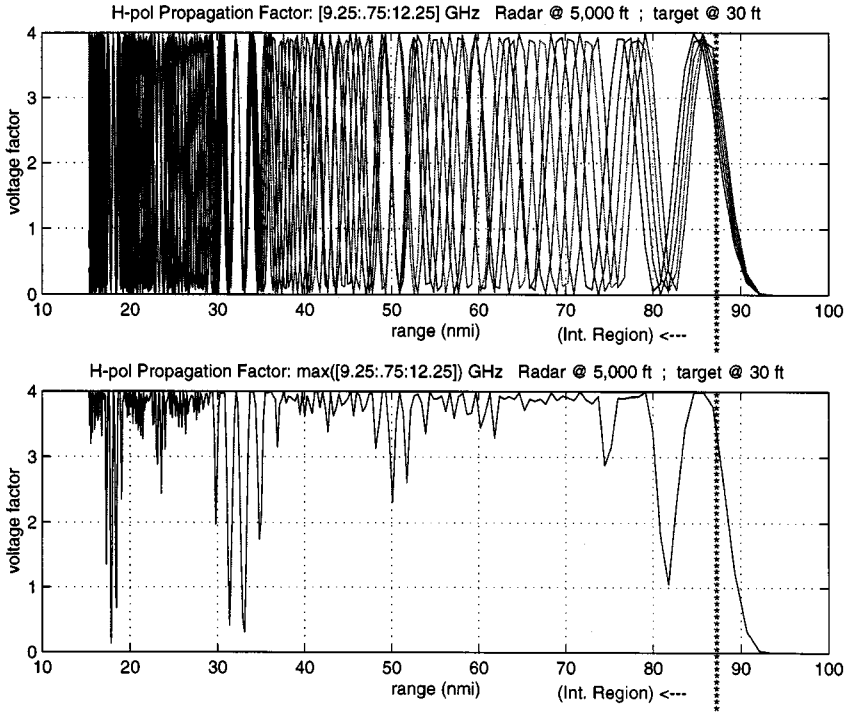

Fig. 13. Lossless CW propagation factor and MPF for five X-band carrier frequencies.

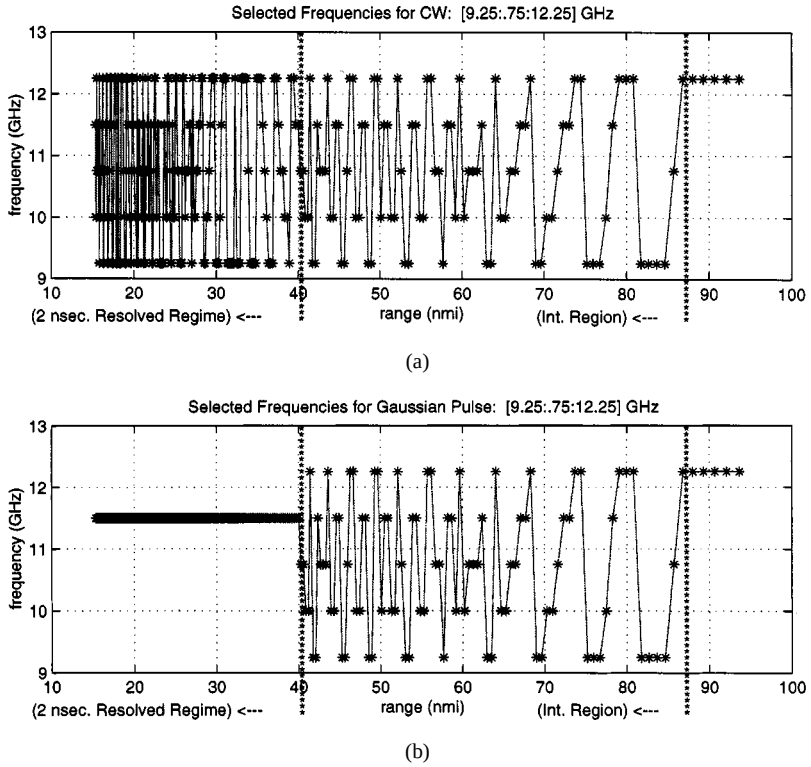

(a)

(b)

Fig. 14. Selected MPF carrier frequencies for (a) CW, and (b) the short Gaussian pulse.

Figs. 11 and 12 illustrate the multipath channel interference effects for the cases of the short Gaussian pulse and linear FM waveforms, respectively. In both cases, the coherent interference causes the voltage propagation factor to vary from zero to approximately three. However, the differences in the modulation characteristics cause shifts in the relative positions of the maxima and minima throughout the range extent. In addition, the spatial frequency of the interference is higher for the linear FM modulation. The spatial frequency characteristics arise from the illumination geometry and the instantaneous frequency of the waveform. The differences in the instantaneous frequency of the two waveform modulation types is important when con-

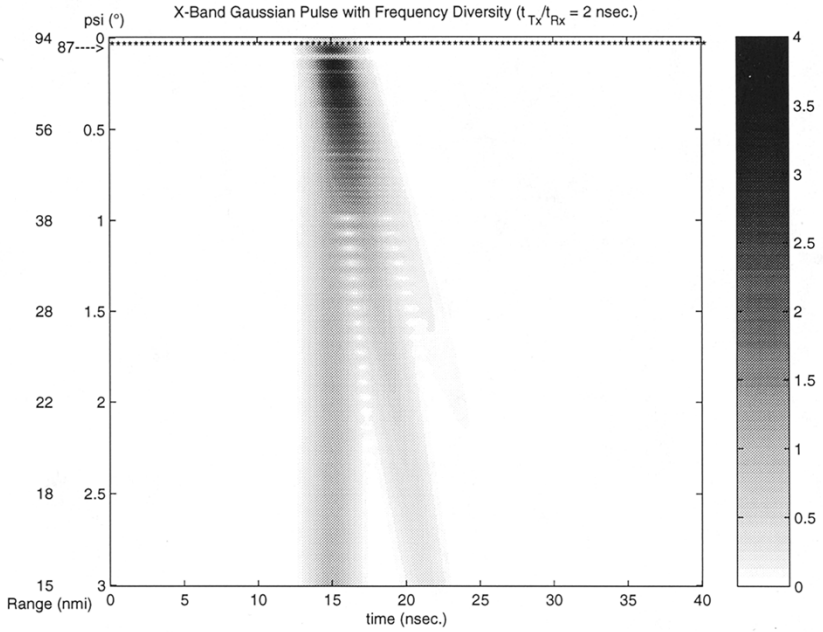

(a)

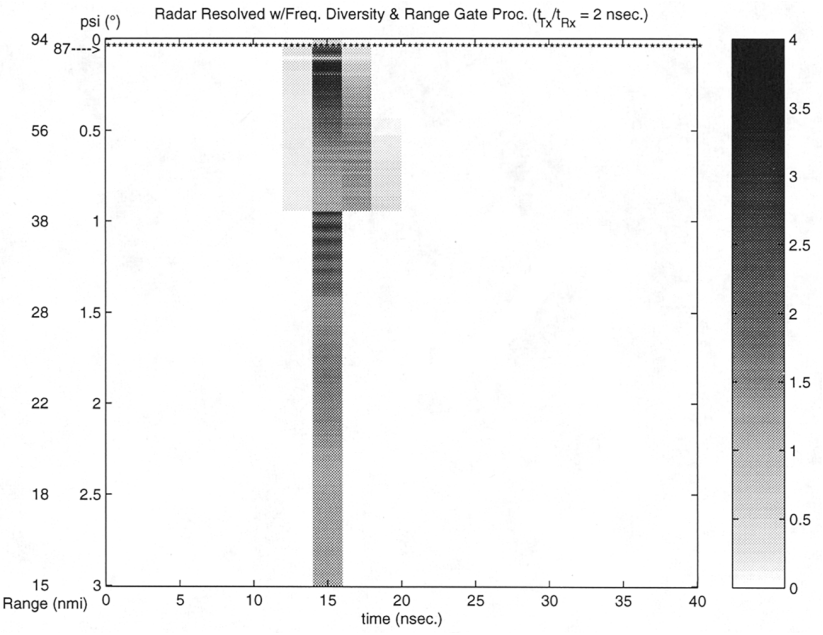

(b)

Fig. 15. Short Gaussian pulse MPF results using (a) frequency diversity and (b) combined with radar resolved range gate processing.

sidering the use of frequency diversity to mitigate the multipath channel.

IV. Multipath Channel Mitigation Considerations

This section considers mitigating the multipath channel in the unresolved and resolved domains of the interference regime. Mitigation in the unresolved domain is based on the utilization of wide-band frequency diversity. To appreciate the utility of frequency diversity in the unresolved domain of the interference regime, consider the lossless CW propagation factor for five X-band frequencies ranging from 9.25 to 12.25 GHz shown in Fig. 13. The top graph in Fig. 13 illustrates the channel interference characteristics for individual carrier frequencies spaced at 750 MHz. The voltage propagation factor is shown as a function of range. The bottom graph in Fig. 13 illustrates the maximum propagation factor (MPF) that results from selecting the largest propagation factor from the set of five carrier frequencies shown in the upper graph. The carrier frequencies that correspond to the MPF for CW operation are shown in Fig. 14(a). Fig. 14(b) identifies the carrier frequencies for the short Gaussian pulse. Note that for basic pulse modulation in the unresolved domain, the desired carrier frequencies are the same as those selected for CW. However, the choice of carrier frequency in the resolved domain is superfluous in the context under consideration. Consequently, the carrier frequency selection is shown to remain constant for ranges less than 40 nmi in Fig. 14(b). For

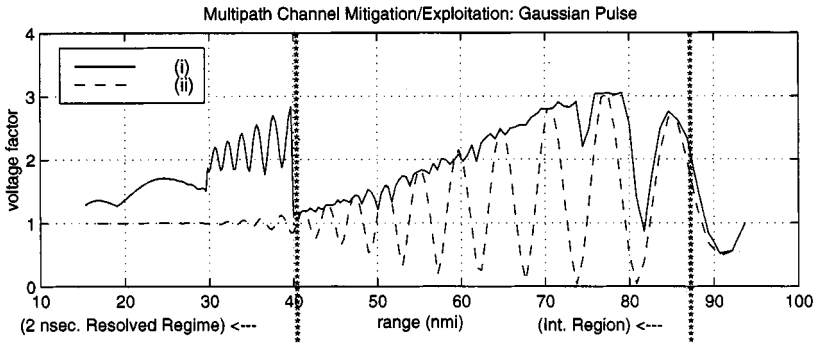

Fig. 16. MPF enhanced (i), and uncompensated (ii) multipath channel.

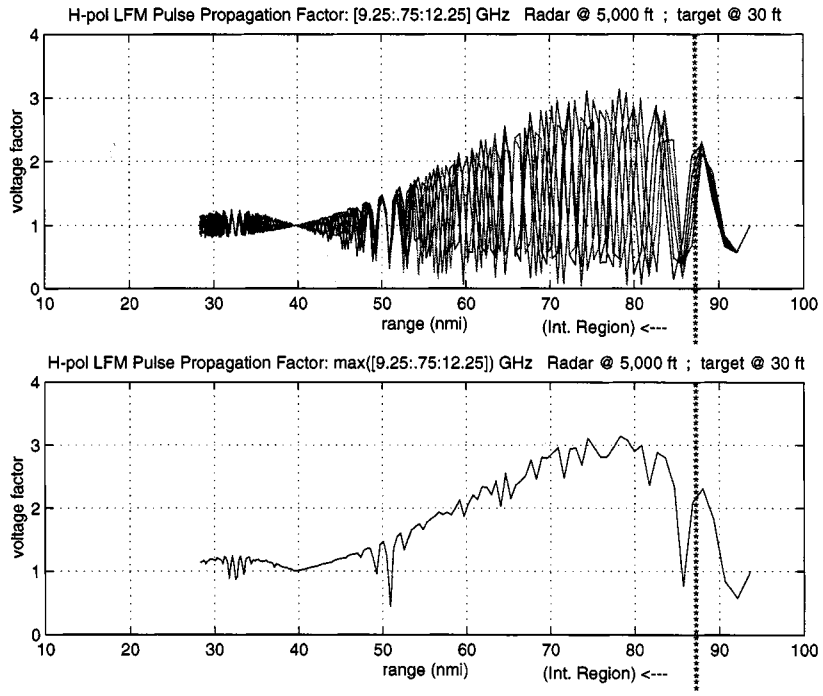

Fig. 17. Linear FM propagation factor and MPF for five X-band carrier frequencies.

ranges less than 40 nmi the specular multipath components are resolved, and coherent superposition of adjacent range bins is possible to combine the components associated with a single platform. While the need to perform a processing step of this type depends on other considerations, it is nevertheless possible to implement with a basic transversal filter. Fig. 15 illustrates the MPF results using the carrier frequencies identified in Fig. 14(b). Fig. 15(a) is a highly time resolved representation of the channel using frequency diversity without processing the resolved domain. Fig. 15(b) represents a radar resolved version of Fig. 15(a) that has also been processed to illustrate the results of coherently combining adjacent range bins in the resolved domain. Fig. 16 is comprised of range cuts through Figs. 11(a) and 15(b) centered on the subject range bin and illustrates the MPF improvement over the uncompensated channel characteristics. Most noteworthy is that free-space performance (corresponds to unity) is maintained through almost the entire range extent, mitigating the channel's deep fade characteristics. In addition, performance over most of the range extent is enhanced relative to free space, where in some cases the voltage improvement factor is as large as 3 ($\sim$9.5 dB in power). Note that the overall deleterious propagation effects of the channel as well as the potential for enhancement are principally a function of the composite complex specular reflection coefficient (A.1).

Directing attention now to the more practical case of linear FM modulation, the instantaneous frequency characteristics of the waveform differ considerably from the short Gaussian pulse waveform. As in the case with short Gaussian pulse modulation, the same five X-band carrier frequencies are considered to mitigate the multipath channel characteristics. However, the carrier frequencies must be considered in combination with the linear FM modulation to characterize the uncompensated channel. The linear FM voltage propagation factor for the uncompensated channel is shown as a function of range in the upper graph of Fig. 17. The lower graph in Fig. 17 illustrates the MPF that results from selecting the largest propagation factor from the set of five carrier frequencies represented in the upper graph. The carrier frequencies that correspond to the MPF for linear FM modulation are shown in Fig. 18(a). Note that the uncompressed linear FM pulse duration is 4 μs and the unresolved domain of the in-

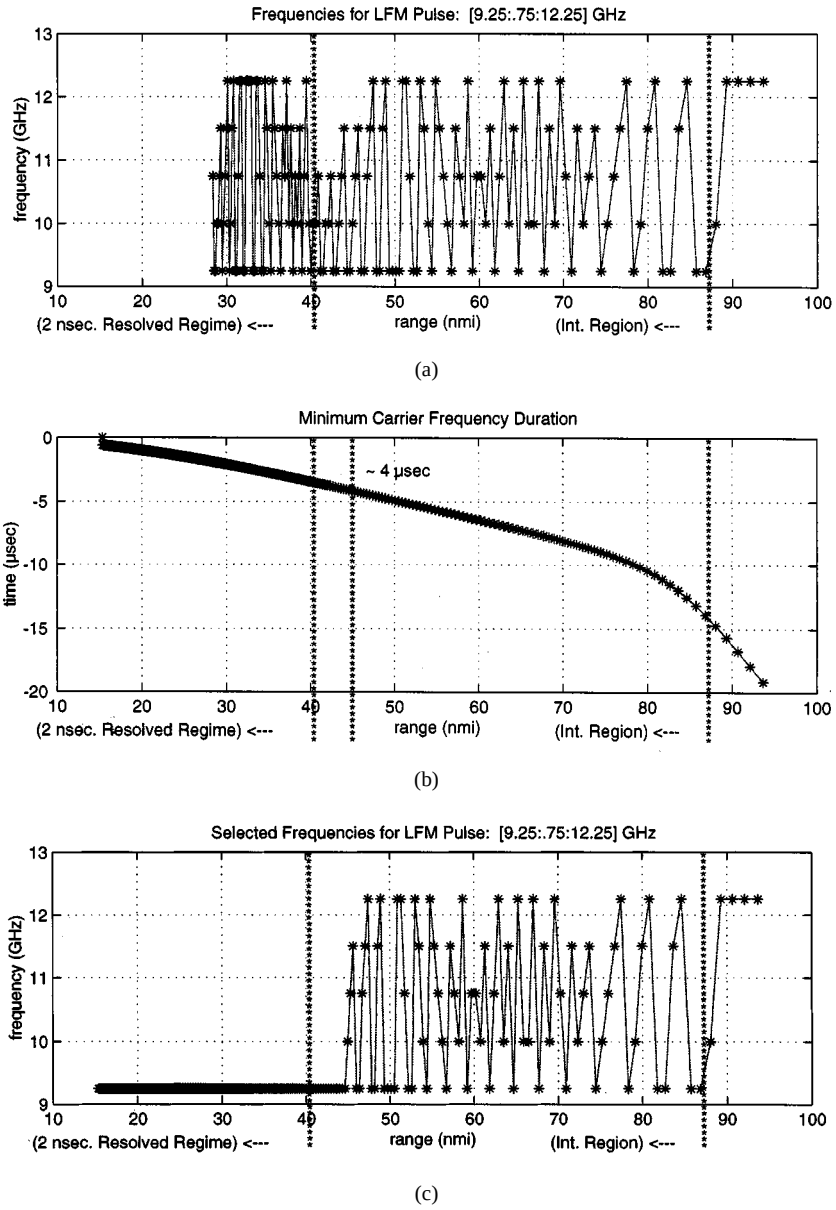

Fig. 18. Linear FM (a) selected MPF carrier frequencies, (b) modulation duration constraints, and (c) selected MPF carrier frequencies subject to modulation duration constraints.

terference regime identified in Fig. 18(a) includes near ranges that are significantly less than the 40 nmi range that are resolved by a 2 ns pulse duration. In addition, the selected MPF carrier frequencies must be constrained to remain constant for the uncompressed linear FM pulse duration so that pulse compression performance is maintained. Fig. 18(b) illustrates the minimum carrier frequency duration for the MPF carrier frequencies shown in Fig. 18(a). The vertical line located at approximately 45 nmi in Fig. 18(b) identifies the 4 μs constraint. Fig. 18(c) identifies the selected MPF carrier frequencies subject to the linear FM duration constraint shown in Fig. 18(b). Fig. 19 illustrates the MPF results using the carrier frequencies identified in Fig. 18(c). Fig. 19(a) is a highly time resolved representation of the channel using frequency diversity without processing the resolved domain. Fig. 19(b) represents a radar resolved version of Fig. 19(a) that has also been processed to illustrate the results of coherently combining adjacent range bins in the resolved domain. Fig. 20 is comprised of range cuts through Figs. 12(a) and 19(b) centered on the subject range bin, and illustrates the MPF improvement over the uncompensated channel characteristics. Also shown in Fig. 20 is the voltage factor that would result if the same carrier frequency selection used for the short Gaussian pulse was also used for the linear FM waveform. The inclusion of this trace illustrates the dependence of the carrier frequency selection on the waveform's instantaneous frequency. As in the short Gaussian pulse case, Fig. 20 indicates that free-space performance is maintained through almost the entire range extent, mitigating the channel's deep fade characteristics. In addition, performance over most of the range extent is also enhanced relative to free-space, with a voltage improvement factor as large as 3 ($\sim$9.5 dB in power) at some ranges (also similar to the short Gaussian pulse case). In contrast to the case of the short

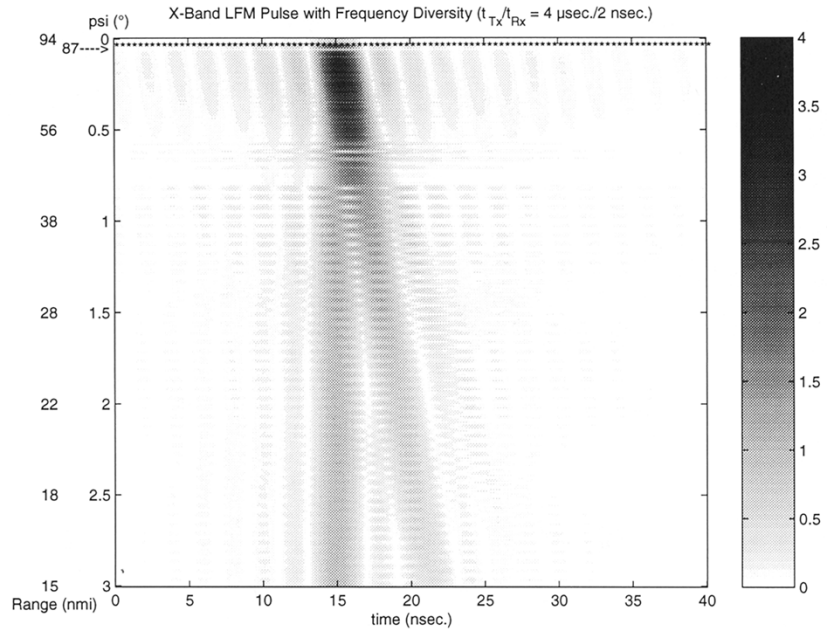

(a)

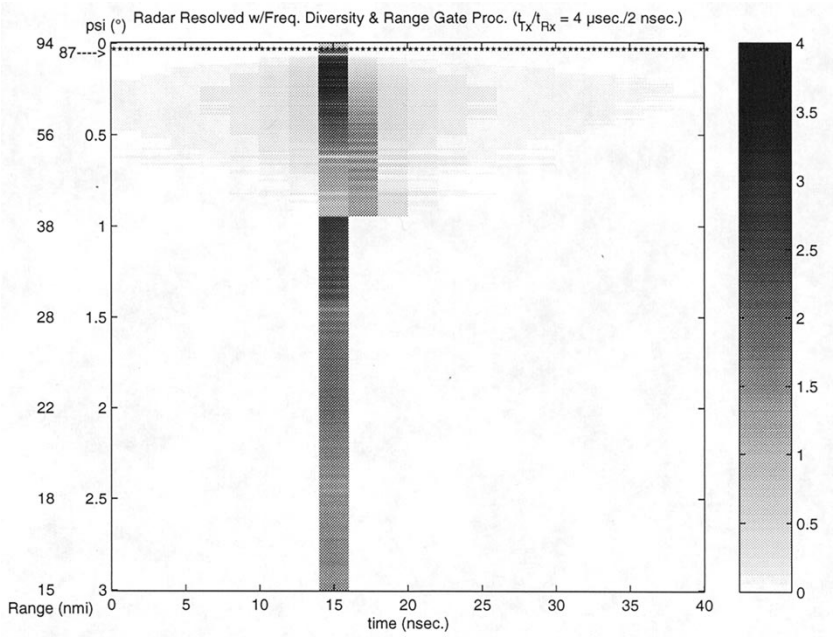

(b)

Fig. 19. Linear FM pulse MPF results using (a) frequency diversity and (b) combined with radar resolved range gate processing.

Gaussian pulse, the 4-μs constraint associated with the linear FM waveform does not allow frequency diversity to be employed in the near range portion of the unresolved domain.

V. Conclusions

Favorable conditions to mitigate and exploit coherent multipath are synonymous with the conditions for the existence of the deleterious aspects of the phenomena. This effort was undertaken to assess the feasibility of mitigating and possibly exploiting a representative specular multipath channel encountered by an airborne wide-band radar sensor performing low-altitude surveillance in a maritime environment. The effort involved the construction of a physically representative multipath channel that included basic considerations for ducting and respected the limitations of characterizing tropospheric propagation phenomena using a geometrical optics solution to the wave equation. The wide-band effects experienced by the individual specular multipath components were included in the distinction of the resolved and unresolved domains of the interference regime. Wide-band frequency diversity was utilized to mitigate and exploit channel effects in the unresolved domain and the possibility of coherently combining adjacent range bins to exploit the resolved domain was shown. While the need to perform a processing step of this type is likely to depend on other considerations, it is nevertheless possible to implement

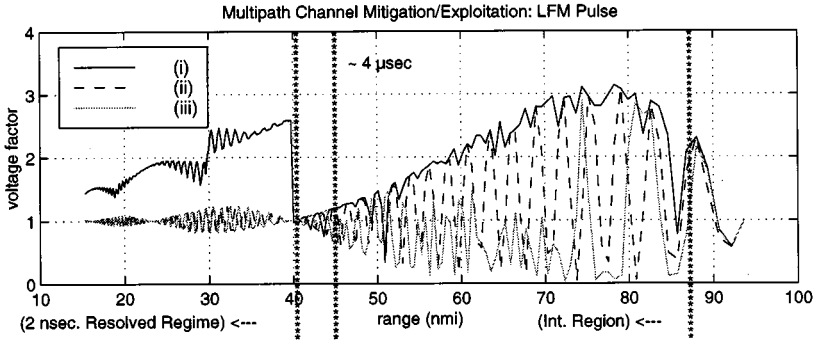

Fig. 20. MPF enhanced (i), uncompensated (ii), and unsuccessfully compensated (iii) multipath channel.

with a basic transversal filter. In addition, the further implications of extended scatterers must be appropriately examined. A short Gaussian pulse and a linear FM waveform were considered for illustration, each having a 500-MHz information bandwidth, and utilized in combination with five X-band carrier frequencies. Most importantly, the consideration of the two modulation types illustrated the carrier frequency selection dependence on a waveform's instantaneous frequency and modulation duration.

The implementation possibilities include a carrier frequency hopping scheme that time interleaves transmissions to interrogate a particular range extent and a simultaneous transmission scheme. The final design of a frequency hopping scheme would have to consider a range of target altitudes and an acceptable compromise may be difficult to achieve under some operating scenarios. Consequently, exclusive use of frequency hopping may be undesirable. A more capable implementation is to simply transmit all carrier frequencies simultaneously and employ a channelized receiver architecture. For example, the frequency diversity and modulation used in this analysis total to a reasonable ≈35% bandwidth. The channelized receiver could be implemented either at RF or digitally. Note that in a simultaneous transmission scheme, target altitude can be inferred from the frequency band dependency of the detection performance. Furthermore, the presence of ducting conditions could also be sensed. A combined frequency hopping and simultaneous transmission scheme is also possible with and without considerations for search and track functions. The final decision would likely result from the aggregate system cost and complexity versus desired performance. Furthermore, while an airborne illumination geometry was considered explicitly, the concepts presented are equally applicable to a ship based illumination geometry with appropriate differences in parameter selection.

In summary, the overall feasibility analysis presented indicates that mitigation and exploitation of a specular multipath channel is possible, provided the radar sensor operational characteristics (bandwidth, frequency diversity, and associated signal processing) are appropriately designed.

APPENDIX

To complete a sufficient physical representation of a maritime multipath channel, additional ocean surface scattering characteristics for the bounce path must be included. As in the case of tropospheric propagation, extensive information on ocean (and rough) surface scattering exists in the open literature (e.g., [9]–[11]). The scattering details considered sufficient for treating the specular reflection characteristics of concern include the Fresnel reflection coefficient $\Gamma(\psi,\epsilon)$, the divergence factor $D_s(R_1,R_2,\psi)$, and an ocean surface roughness factor $r_s(\sigma_H,\psi)_{rms}$ that accounts for the random nature of the surface fluctuations. The corresponding composite complex specular reflection coefficient is given by

$$\rho_{rms} = r_s(\sigma_H,\psi)_{rms} D_s(R_1,R_2,\psi)\Gamma(\psi,\epsilon) \tag{A.1}$$

where ψ is the grazing angle, ϵ is the complex permittivity, and σ_H is the standard deviation of the ocean surface height. Note that in general the complex reflection coefficient consists of specular (coherent) and a diffuse (incoherent) scattering components. However, as mentioned previously, this work is interested in coherent interference between the direct and ocean surface reflected wave components and the reflection must be highly specular for the interference phenomena to exist. The complex reflection coefficient (A.1) is linked to the environmental conditions through the standard deviation of the ocean surface height σ_H and the complex permittivity ϵ. The significant wave height H_s (average of the one-third highest waves) is related to the standard deviation of the ocean surface height according to $\sigma_H = 0.25H_s$ [11]. The significant wave height can be readily related to wind conditions and sea state. The complex permittivity accounts for salinity and finite conductivity, and is a function of frequency and temperature [10].

The individual factors that comprise (A.1) are given by

$$r_s(\sigma_H,\psi)_{rms} = e^{-2k\sigma_H \sin\psi} \tag{A.2}$$

$$D_s(R_1,R_2,\psi) = \left(1+\frac{2R_1R_2}{a_e(R_1+R_2)\sin\psi}\right)^{-1/2} \cdot \left(1+\frac{2R_1R_2}{a_e(R_1+R_2)}\right)^{1/2} \tag{A.3}$$

and

$$\Gamma(\psi,\epsilon) = \begin{cases} \dfrac{\epsilon\sin\psi - \sqrt{\epsilon-\cos^2\psi}}{\epsilon\sin\psi + \sqrt{\epsilon-\cos^2\psi}}, & \text{V-pol} \\ \dfrac{\sin\psi - \sqrt{\epsilon-\cos^2\psi}}{\sin\psi + \sqrt{\epsilon-\cos^2\psi}}, & \text{H-pol.} \end{cases} \tag{A.4}$$

The validity of the multipath channel considerations is confined to the interference regime. In particular, the divergence factor (A.3) is derived using geometrical optics, and is no longer valid near the horizon. The grazing angle regime associated with the geometrical optics limit in describing the interference regime is given by [3]

$$\psi \geq \tan^{-1}[(ka_e)^{1/3}]. \tag{A.5}$$

REFERENCES

[1] M. I. Skolnik, Ed., *Radar Handbook*. New York: McGraw-Hill, Inc., 1990.

[2] D. E. Kerr, *Propagation of Short Radio Waves*. New York: MIT Radiation Lab. Seri., 1951, vol. 13.

[3] K. A. Norton, "The calculation of ground-wave field intensity over a finitely conducting spherical earth," *Proc. IRE*, vol. 19, no. 12, pp. 623–639, Dec. 1941.

[4] H. V. Hitney, J. H. Richter, R. A. Rappert, K. D. Anderson, and G. B. Baumgartner, Jr., "Tropospheric radio propagation assessment," *Proc. IEEE*, vol. 73, pp. 265–283, Feb. 1985.

[5] K. D. Anderson, "Radar detection of low-altitude targets in a maritime environment," *IEEE Trans. Antennas Propagat.*, vol. 43, pp. 609–613, June 1995.

[6] G. D. Dockery, "Modeling electromagnetic wave propagation in the troposphere using the parabolic equation," *IEEE Trans. Antennas Propagat.*, vol. 36, pp. 1464–1470, Oct. 1988.

[7] C. L. Rino and H. D. Ngo, "Forward propagation in a half space with an irregular boundary," *IEEE Trans. Antennas Propagat.*, vol. 45, pp. 1340–1347, Sept. 1997.

[8] D. F. Gingras, P. Gersoft, and N. L. Gerr, "Electromagnetic matched-field processing: Basic concepts and tropospheric simulations," *IEEE Trans. Antennas Propagat.*, vol. 45, pp. 1536–1545, Oct. 1997.

[9] P. Beckmann and A. Spizzichino, *The Scattering of Electromagnetic Waves from Rough Surfaces*. New York: Macmillan, 1963.

[10] F. T. Ulaby, R. K. Moore, and A. K. Fung, *Microwave Remote Sensing*. Norwood, MA: Artech House, 1986, vol. III.

[11] J. R. Apel, *Principles of Ocean Physics*. New York: Academic, 1987.

Joseph G. Teti, Jr. (M'91) received the B.S. degree from Drexel University, Philadelphia, PA, in 1985, and the M.S.E. and Ph.D. degrees from the University of Pennsylvania, Philadelphia, in 1989 and 1991, respectively, all in electrical engineering.

From 1985 to 1987, he was a Staff Engineer with Flam and Russell, Inc., Horsham, PA. From 1987 to 1992 he was with the Naval Air Development Center (NADC), Warminster, PA. From 1989 to 1991 he was on leave as an NADC Ph.D. Fellow at the Moore School of Electrical Engineering, University of Pennsylvania, Philadelphia. In 1992 he returned to industry and in 1995 he founded Lambda Science, Inc., Wayne, PA, where he is currently the Chief Scientist. His research interests are broad and span topic areas that pertain to the design and application of advanced sensors. He has experience in advanced radar sensor system design and applications that include instrumentation, surveillance, tactical, surface search, HF over-the-horizon, and synthetic aperture radar. His experience also includes RF hardware covering areas from devices to antennas, theoretical, and applied advanced signal processing techniques that emphasize the extraction and utilization of available sensor information, and the analysis of propagation and scattering phenomenology for the purposes of mitigation and/or exploitation.

Dr. Teti is a member of several IEEE societies, the Society of Industrial and Applied Mathematics (SIAM), the American Geophysical Union (AGU), the Association of Old Crows (AOC), Tau Beta Pi, and Sigma Xi.